The Astronomical Journal, 124:619–634, 2002 July

THE LAS CAMPANAS INFRARED SURVEY CAMERA

S. E. Persson,[1] D. C. Murphy,[1] S. M. Gunnels,[2] C. Birk,[1] A. Bagish,[1] and E. Koch[3]
Received 2001 September 12; accepted 2002 April 2

ABSTRACT

The Las Campanas Infrared Survey Camera is a near-infrared (1.0–2.5 μm), wide-area instrument used to detect and measure the photometric properties of galaxies out to large redshifts, $z > 2$. The camera, a modified Offner 1 : 1 reimaging optical system, is mounted at the f/7.5 focus of the 2.5 m du Pont Telescope. The detectors are four Rockwell 1024 × 1024 HgCdTe (HAWAII) arrays operating at a scale of 0.″20 pixel^{-1}. With four telescope pointings, the instrument produces a pipelined mosaic of J, H, or K_s images 13′ × 13′ on the sky, with a measured point-spread function as good as 0.″38 FWHM. The good imaging quality results in part from fast tip-tilt guiding on stars within a 9′ × 9′ field centered on the optical axis of the telescope. Appropriately bright guide stars are found within 2 s from a catalog of 5×10^7 stars and presented as a "finding chart" to the observer. The optical, mechanical, and thermal design choices and their associated engineering implementations are discussed in some detail. The detector readout electronics, the automatic data acquisition and control system, and our data reduction pipeline are also described. The design goals of the camera—excellent imaging quality and throughput, low flexure and internal background, and 5 Hz on-axis guiding, are all realized and quantified.

Key words: instrumentation: miscellaneous — techniques: photometric

On-line material: color figures

1. INTRODUCTION

Recent rapid improvement in the quality and size of near-infrared imaging array detectors has led to great advances in many areas of astronomy, and the time is opportune to apply them to ambitious surveys. The camera described in this paper has been developed for the purpose of conducting deep ($K_s \sim 21$) and wide ($\sim$1 deg^2) surveys at a critical spatial sampling of $\sim$0.″2 pixel^{-1}. The primary scientific motivation behind the instrument definition is the fact that it has become possible to create samples of distant galaxies selected in the near-infrared, that is, between 1 and 2.4 μm. Extending the camera design to include the K_s passband (1.99–2.32 μm) increases the engineering challenges, but the scientific gains are compelling. For example, at this wavelength the photometric properties of galaxies, even to $z \sim 2$, are relatively unaffected by rather weak bursts of star formation superposed on an underlying passively evolving stellar system. The 2 μm light provides the best measure of the stellar mass, and thus a comprehensive K_s survey should yield a reliable picture of where the galaxy masses are.

Carnegie Observatories embarked on the construction of the camera in 1997. We developed a plan with colleagues at the University of Cambridge whereby Carnegie would build a cold optical reimaging system and attach the Cambridge four-array dewar (CIRSI; Beckett et al. 1998) to it. This paper describes our camera design and provides measured performance data. The main features are operation out to the K_s band, fast (5 Hz) tip-tilt guiding close to the telescope axis, critical sampling for stellar images, i.e., 0.″20 pixel^{-1}, four separated square fields totaling 43 arcmin^2 in sky area, automatic data acquisition, and pipelined data reduction. Each of these features is described in detail, along with explanations of our engineering and design choices. We began routine K_s survey observing on the 2.5 m du Pont Telescope at Las Campanas in 2001 March.

[1] Observatories of the Carnegie Institution of Washington, 813 Santa Barbara Street, Pasadena, CA 91101; persson@ociw.edu, david@ociw.edu, birk@ociw.edu, alanb@ociw.edu.

[2] Paragon Engineering, 18231 Old Ranch Road, Tehachapi, CA 93561; paragoneng@cybersurfers.net.

[3] Dedicated Micro Systems, 632 South Park Rose Avenue, Monrovia, CA 91016; ekoch@linkline.com.

2. CAMERA DESIGN

2.1. *Passbands, Detector Arrays, and Pixel Scales*

The camera's optical design was chosen according to criteria established primarily by our science goals. As discussed above, it was considered essential that the camera work in the K_s band. This single choice greatly increases the instrument's cost and complexity because of the requirements imposed on the thermal and vacuum designs of the system. Baffling of thermal radiation from high-emissivity areas within the telescope is basic to good performance at K_s. An effective internal baffle also automatically ensures a system that is well baffled against sky radiation (particularly OH emission in the J and H bands), to which the focal plane is directly exposed on unbaffled Cassegrain telescopes. Thus, the baffle and optics were to be mounted within an evacuated dewar and operated at a temperature sufficiently low that negligible excess thermal background from the camera itself would be added.

The choice of array manufacturer was straightforward: Rockwell's HAWAII HgCdTe arrays (1024 × 1024 18.5 μm pixels) were of high quality and high quantum efficiency, were affordable, and were available.

Typical near-infrared image quality at the 2.5 m telescope ranges from about 0.″38 to 0.″9, with a median $\sim$0.″5, full width at half-maximum (FWHM). The scale of the f/7.5 Ritchey-Chrétien configuration is 0.″20 per 18.5 μm HAWAII pixel, which suggested that critical image sampling could be achieved without focal reduction. Although this spatial resolution is perhaps slightly too high for surveying distant galaxies, it is ideal for stellar photometry and has

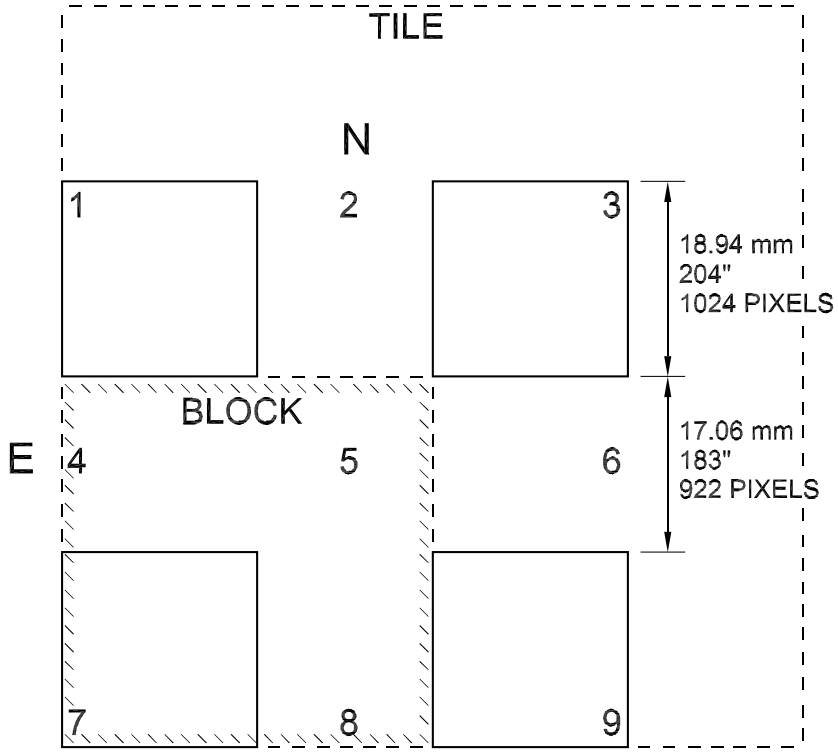

FIG. 1.—Geometry of the four Rockwell detector arrays. The physical and angular sizes and spacings are indicated. Four telescope pointings map a "block" with each detector, and four such blocks make up a "tile." The numbers 1 through 9 refer to the locations of the spot diagrams in Fig. 3.

the other practical advantage of facilitating the removal of pixels hit by cosmic rays.

For wide-area surveys with multiarray cameras, the geometries that produce nearly uniform signal-to-noise ratio images have the arrays spaced by either a very small number of pixels or roughly the width of an array. For the latter case with four arrays, four telescope pointings serve to fill in the spaces between the arrays. The main disadvantage is that several engineering challenges are introduced by having a field 50% larger than for the zero-spacing scheme. The practicalities of the Rockwell arrays, specifically their packaging, led the Cambridge group to adopt, sensibly, a spacing of 90% of an array. Figure 1 sketches the geometry, and Table 1 gives the essential array and camera parameters.

A number of other design considerations entered our planning: High throughput is essential for survey work. The

TABLE 1
DETECTOR AND CAMERA PARAMETERS

Parameter	Value	Parameter	Value
Detector		Camera	
Manufacturer	Rockwell Science Center	Independent signal chains	16 units
Type	HAWAII	Frame clocking time	2 s
Material	HgCdTe on sapphire	Pixel scale on sky	$0\farcs199$ pixel^{-1}
Spectral response	0.85–2.5 μm	Detector format on sky	1024×1024; four detectors total
Format	1024×1024 pixels	Camera format on sky	Four $197'' \times 197''$ frames at corners of $560'' \times 560''$ square
Pixel pitch	18.5 μm	Mirror surfaces	4
Capacity	$>60{,}000\ e^-$	Glass surfaces	6
Maximum data rate	1 MHz	Filters	J, H, K_s; nine total
Operating temperature	77 K	Guide field	$560'' \times 560''$
Dark current	$<0.15\ e^-\ s^{-1}$ at 77 K $<0.01\ e^-\ s^{-1}$ at 60 K	Tip-tilt guide rate	$\sim$10 Hz
Quantum efficiency	70% at 2.2 μm 60% at 1.2 μm		
QE dispersion	$\approx$5%		
Read noise	$<15\ e^-$ per double read		
Bad-pixel count	<0.02%		

extent of the field required that the intrinsic coma and astigmatism of the telescope be corrected. Finally, we were obliged to provide telescope guiding capability, as it was not practical to use any of the existing telescope guider systems.

2.2. *Optical Design and Materials*

The above constraints and considerations suggested the Offner 1 : 1 reimager (Offner 1975) as a suitable basis for the camera optical system. This design, originally invented for semiconductor photolithographic applications, is well suited for use as a reimager in the infrared when 1 : 1 reimaging is appropriate (Murphy 1994; Murphy et al. 1995). The preceding references give detailed discussions of the Offner, which we summarize only briefly here.

The basic (" pure ") Offner consists of two spherical mirrors, one concave and one convex, that share a common center of curvature. In Figure 2, M1 and M3 are sections of the concave mirror, and M2 is the convex one. The Offner reimages one focal plane to another through three reflections, two off the same concave mirror and one off the convex mirror. The distance from the telescope focal plane (the object) to concave mirror M1 is equal to the radius of curvature of M1. Likewise, the image distance (from M3) is equal to the radius of curvature of M3. The image of an object near infinity—in our case, the telescope exit pupil—is formed by M1 at a distance equal to one-half its radius, which is where convex mirror M2 is located. Very simple considerations based on symmetry show that the Offner has the remarkable attribute of being free from *all* primary aberrations. This fact, which makes it an inherently wide-field system, coupled with the naturally high throughput achieved using reflective optics in the infrared, the relatively low number of reflections, and the tolerant nature of a spherical system, made the Offner a natural choice.

Our *specific* camera optical system is a variant of the pure Offner, modified to meet our needs. The design is presented in Table 2 and Figure 2. The first modification involved separating the concave Offner mirror into two spherical mirrors—M1 and M3—with independent radii of curvature, vertex locations, and tilts. This separation facilitates the simultaneous optimization of both focal- and pupil-plane images and keeps the optical elements more manageable in size. The second variation places a refractive field corrector in the converging beam ahead of the imaging arrays. Its purpose is to correct telescope coma and astigmatism, which, if left uncorrected, would appear at the 3 pixel level at the corners of our field. The corrector is an all-spherical doublet of infrared-grade fused silica. Among the important constraints on our implementation of the Offner was the requirement that the image of the telescope exit pupil formed by M1 on convex Offner mirror M2 be sharp enough that a cold stop could be placed at this location to effectively baffle

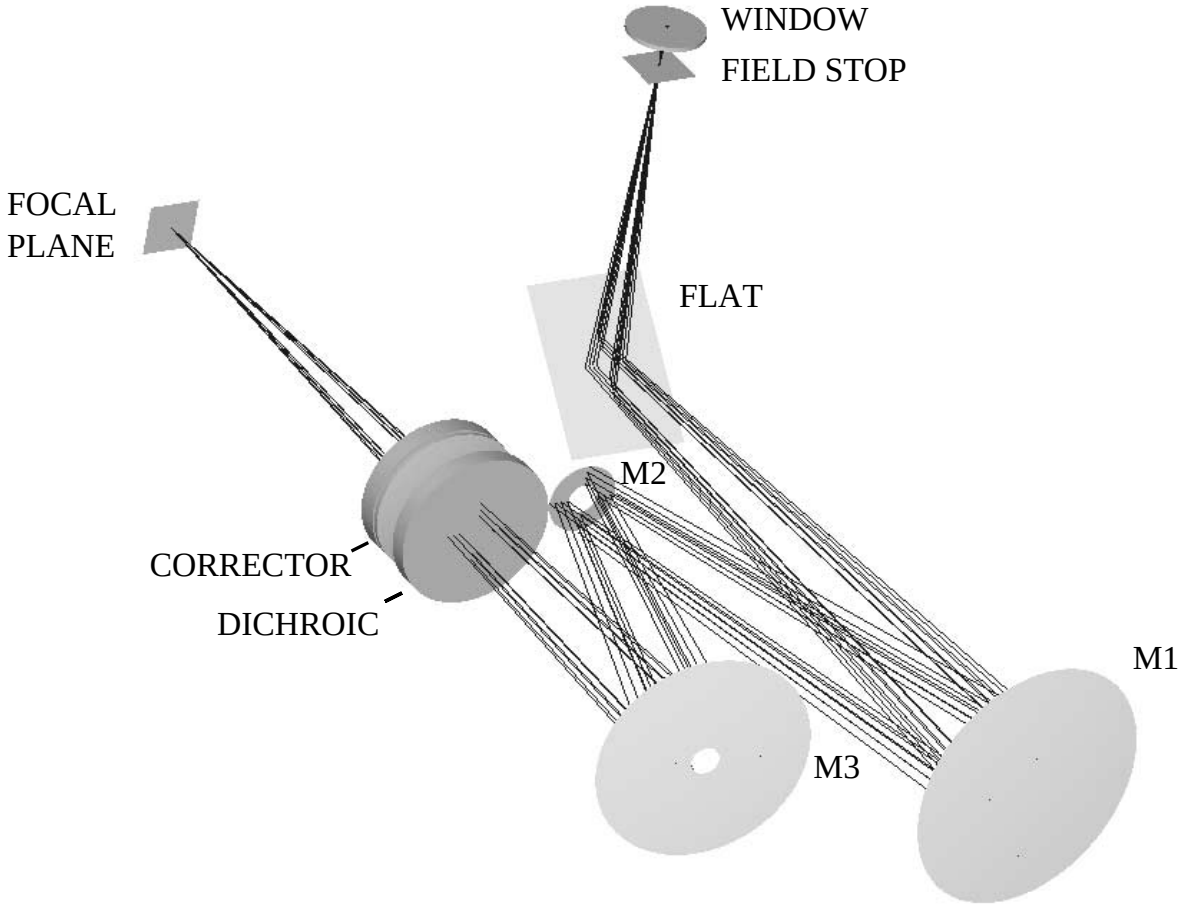

FIG. 2.—Schematic view of our variant of the Offner optical system. Telescope focus is at the field stop, M1 and M3 are spherical mirrors concave toward M2, and M2 is a spherical mirror convex toward M1 and M3. Optical light reflected off the dichroic exits the camera through the hole in M3 to a guide camera. See text for further explanation.

TABLE 2
DETAILED OPTICAL DESIGN

Surface	Radii[a] (mm)	Displacement[b] (mm)	Tilt[c] (deg)	Thickness (mm)	Glass	Index[d]	Diameter[e] (mm)
Telescope primary[f]	−15240.19	...	...	...	Mirror	...	2540
Air space	...	...	...	5156.22	...	...	...
Telescope secondary[g]	8224.63	...	...	...	Mirror	...	953
Air space	...	...	...	6100.73	...	...	...
Window	...	...	...	5.08	Sapphire	1.74535	83.3
Air space	...	...	...	42.52	...	...	...
Field stop	...	...	...	...	...	...	56 × 56
Air space	...	...	...	356.73	...	...	...
Flat[h]	...	...	...	...	Mirror	...	132 × 186
Air space	...	...	...	864.80	...	...	...
Mirror M1	−1226.86	...	7.02	...	Mirror	...	273.2
Air space	...	...	...	635.68	...	...	...
Mirror M2	578.14	159.03	−0.90	...	Mirror	...	75.8
Air space	...	...	...	493.96	...	...	...
Mirror M3	−1087.24	300.00	−7.94	...	Mirror	...	232.4
Air space	...	...	...	466.60	...	...	...
Dichroic	...	300.00	...	20.00	Silica	1.44342	168.4
Air space	...	...	...	30.00	...	...	...
Corrector element 1	405.67	300.00	...	13.60	Silica	1.44342	161.4
	−13888.00	...	...	...	...	...	...
Air space	...	...	...	4.22	...	...	...
Corrector element 2	−4909.40	300.00	...	13.60	Silica	1.44342	161.4
	396.16	...	...	...	...	...	...
Air space	...	...	...	536.80	...	...	...
Focal plane	...	300.00	...	...	...	...	...

[a] Negative radius indicates concave surface.
[b] Tilt sense is such that M1 and M3 point toward M2.
[c] Shift of surface vertex with respect to telescope optical axis.
[d] Calculated at center of *H* bandpass.
[e] Full aperture diameter or rectangular footprint.
[f] Asphere with conic constant −1 and sag = $(-6.5617 \times 10^{-5})y^2 + (1.835 \times 10^{-14})y^4$ mm.
[g] Asphere with conic constant −1 and sag = $(-1.818 \times 10^{-4})y^2 + (1.743 \times 10^{-11})y^4$ mm.
[h] Folds beam 90°.

thermal radiation from the high-emissivity areas in the exit pupil.

The above considerations were applied as ray-tracing constraints, and a final optical design was developed using the ZEMAX ray-tracing package (Focus Software, Inc.; the various vendors that we have used in this project are listed in Table 9). The design included an accurate prescription for the 2.5 m telescope's optics (Bowen & Vaughan 1973).

With reference to Figure 2, the f/7.5 telescope beam enters the dewar through a window and comes to focus at the field stop. The diverging beam is redirected into the camera via a flat, where it strikes concave mirror M1, convex mirror M2, and concave mirror M3. A cold baffle is placed at the front surface of M2; it has the shape of the telescope primary mirror (exit pupil), with its central hole and secondary mirror spiders. The beam reflected from M2 strikes M3 and converges at f/7.5 toward the detector. A novel feature of our design, used for guiding, is the dichroic. This optic (Barr Associates, Inc.) reflects light shortward of 0.9 μm; the converging *optical* beam is thus directed through a small hole in M3, where it exits the dewar through a dewar window and forms an optical focus used for fast guiding. The dichroic is gimballed and tilts under computer control through an angle of $\pm 1\overset{\circ}{.}8$ north-south and east-west. It is thereby possible to steer the field received by the guide camera ($\sim 95'' \times 125''$) to any point in the (larger) available field at the telescope focal plane. As shown in Figure 1, this field is $9\overset{'}{.}1 \times 9\overset{'}{.}1$. The guide-camera frame rate is 30 Hz, and image centroids of field stars are computed at this rate. Correction signals processed through a proportional-integral servo loop are then used to tip-tilt mirror M2 at ~5 Hz so as to correct for image motion. With the present camera, stars brighter than *R* magnitude ~15 are adequate for fast guiding. After passing through the dichroic, the infrared photons pass through a doublet field corrector before entering a separate liquid-nitrogen dewar that houses the detector arrays.

The rather bright stellar magnitude of usable guide stars results from light losses at the image-intensifier front end of the guide camera (Xybion Corp.; quantum efficiency ~25%) and from the coating on a small cold filter just ahead of the Xybion. This coating was designed to block 2 μm photons from entering the light path through the window, and it proved to be difficult to maintain high transmission of the coating at optical wavelengths. In practice, the guide-star brightness limit has never been a problem. This confirmed a number of numerical experiments we carried out, wherein we inspected randomly chosen $9' \times 9'$ fields in our guide-star catalogs. We expected, on this basis, that we would only rarely (<2% of the time) fail to find a sufficiently bright guide star near the Galactic poles.

The theoretical performance of the telescope-camera optics-filter combination is illustrated in Figure 3, where polychromatic spots at the center, edges, and corners of

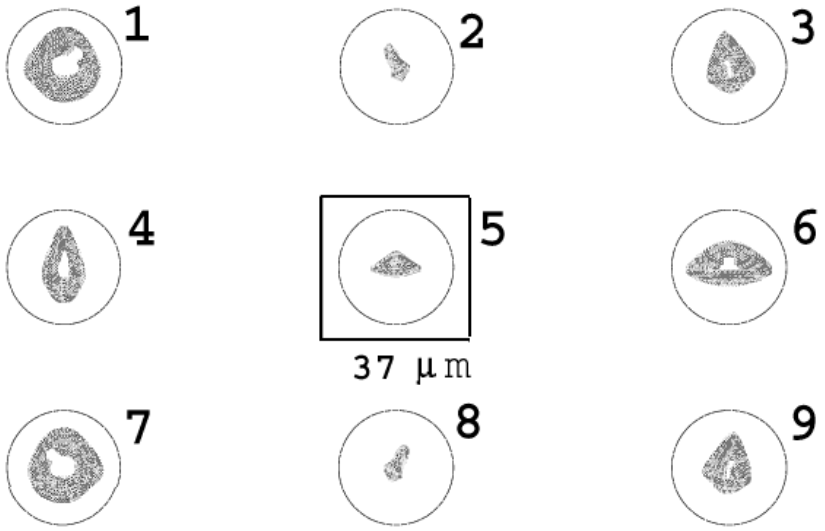

FIG. 3.—Theoretical polychromatic (1.2–2.3 μm) spot diagrams for the telescope-camera system. The circles indicate the first Airy dark ring at 1.65 μm. A scale bar 2 pixels in length (i.e., 37 μm) is also shown. The field locations for the spots are indicated in Fig. 1.

the four-detector field are displayed. These field locations (numbered 1 through 9) are indicated in Figure 1. The circles indicate the first dark ring of the Airy diffraction pattern at 1.65 μm, and the central square indicates a 2×2 pixel region. The design is clearly very well corrected and within a factor of 2 of being diffraction limited.

The image of the telescope pupil formed at M2 is soft compared with the focal-plane images. By ray-tracing a series of object points placed at the primary mirror, we found a maximum spot size $\sim$400 μm at M2. This number sets the size of the baffle at M2, as discussed in § 2.7.

Previous experience with two Offner systems led us to again choose Zerodur coated with protected silver for the mirrors (obtained from JML Optical Industries, Inc.). Infrared-grade fused silica was chosen for both corrector elements and the dichroic. Sapphire was chosen for the dewar window for three reasons: First, it has rather high thermal conductivity and thus will not tend to develop a lower temperature region at its center due to the imbalance in thermal load from inside and outside the dewar. This reduces the chances of condensation or icing of the window under ambient conditions of a small dew-point depression. A temperature profile model was developed and a thickness of 5 mm was chosen. According to the model, no central temperature depression can exceed 2°C below ambient. Second, sapphire can be cheaply and effectively antireflection-coated with a single quarter-wave layer of MgF_2. The wavelength chosen for 100% transmission was centered at 1.65 μm. Although sapphire is birefringent at certain angles, our window crystal (Crystal Systems, Inc.) was grown so that the window operates at essentially non-birefringent angles. Finally, sapphire has high stiffness and thus can be made physically thin compared with other dewar window glasses.

2.3. *Thermal Considerations*

Many of the thermal and mechanical design choices followed from noting that the temperature of the camera optics need not be as cold as $\sim$77 K, which is necessary to operate the detectors. The thermal background in the K_s passband at 2.2 μm of a model instrument was computed and compared with that expected from the telescope. We assumed a very clean (emissivity 0.05) and cold (0°C) model telescope. Using nominal reflectivities for the Offner mirrors and refractive elements (see § 5), we calculated that −40°C is sufficiently cold that the instrument could add at most only a few percent to the telescope background. This is a conservative estimate because under normal telescope operating conditions, the K_s background incident on the dewar window is $\sim$10 times higher than in the model. The actual conditions include an ambient temperature of 12°C, more realistic mirror emissivities (each $\sim$0.10), and sky emission.

An important potential contributor to the instrument background is the pupil-plane mask, which absorbs radiation from warm structures behind the central hole and around the periphery of the primary mirror. Because the detectors view this mask surface directly, it must be cold, correctly sized, and of low reflectivity. Another potential contributor to excess instrument background is radiation from surfaces (as seen by the detector) originating at angles well outside the f/7.5 beam (plus annular mask) subtended at M2. To block radiation from these 233 K surfaces, we attached a baffle snout to the cold (77 K) interior of the detector dewar. It projects into the space between the corrector and detector. The final contributor is the hole in M3, which could allow radiation entering the dewar through the guide-camera window to strike the detector. This radiation was blocked with a heat mirror (Barr Associates) attached to the space frame. It has adequate transmission shortward of 1 μm and only a few percent transmission longward.

The physical size of the optical layout prompted us to investigate mechanically efficient space-frame concepts for mounting the optics. In order to ensure rather small focus shifts and misalignments of the optics when cooling from room temperature to −40°C, we elected to build the space frame of Invar. (Invar is a high nickel content steel whose coefficient of thermal expansion is 25 times smaller than that of aluminum.) In addition, an Invar structure reduces misalignments due to steady state thermal *gradients*. The Zerodur mirrors shrink essentially 0% going from room temperature to −40°C, so the optics can be aligned at room

temperature and neither shifts nor thermal gradients in operation are ever a problem.

2.4. *Detailed Mechanical Design*

The design was conceived as consisting of three substructures: the Invar space frame (ISF) to mount the optics, a vacuum dewar to enclose the ISF, and a camera support structure (CSS), which would attach the outside of the vacuum dewar to the Cassegrain instrument mounting ring of the telescope.

Prior to commencing the detailed mechanical design, we performed an analysis of the ZEMAX spot diagrams for decenters, focus shifts, and tilts of all system components. Applying stringent criteria to the allowable total of all image degradations (<20% degradation of the average ZEMAX spot size), we derived a set of tolerances for misalignments of each optical element. There are 57 degrees of freedom, which, for simplicity, we assumed would add in quadrature. The resultant budget set the flexure goals for the finite-element analysis (FEA) design calculations of the ISF.

The total error budget of the optical point-spread function (PSF) also involves manufacturing problems, for example, incorrect mirror radii and uncertain optical index data for the refractive elements. Combining all known sources of error, we arrived at a set of mechanical and thermal specifications for a detailed design of the optical elements, the ISF, the vacuum dewar, and the CSS. The practical issue of aligning the optics is crucially important and is discussed below.

The goals of the mechanical design were as follows: (1) maintain surface figure and alignment of the optics subject to rotations under gravity loading, vacuum loading, and temperature changes; (2) minimize rigid-body motions of the system as the telescope moves, which are manifested as pointing errors; (3) ensure safe stresses in the dewar under vacuum loading; (4) minimize overall weight. In support of these design goals, 32 FEA models of the CSS-dewar-ISF system were created and solved.

The ISF was made by welding 1.6 cm square Invar bars and several Invar plates; Figure 4 shows a diagram. The bare structure is approximately $33 \times 64 \times 118$ cm in size and weighs 62 kg. The ISF is kinematically defined to the vacuum dewar via six rod flexures made of hardened steel. These flexures have minimal stiffness against bending and maximal stiffness against compression or stretching. The result is that any distortions or motions of the outer dewar induced by thermal, gravity, or vacuum changes cause the ISF-optical system to move as a rigid body.

The dewar (Fig. 5) has three mechanical functions: it provides a vacuum barrier between the optical system and the atmosphere, it transfers the support of the ISF to the telescope via the rod flexures and CSS, and it provides mounting surfaces for the detector dewar and other modules. The dewar is a welded, machined, and mechanically stiffened box made from 6061-T6 aluminum plates. Its inside dimensions are $\geq$1.5 cm larger than the outside dimensions of the ISF, and it weighs 110 kg. We designed the stiffeners to limit the plate deflections under vacuum loading to $\leq$0.7 mm.

The CSS (Fig. 5) is a space-frame structure of welded 3.2 cm square steel tubing; it is 43 cm deep and weighs 39 kg.

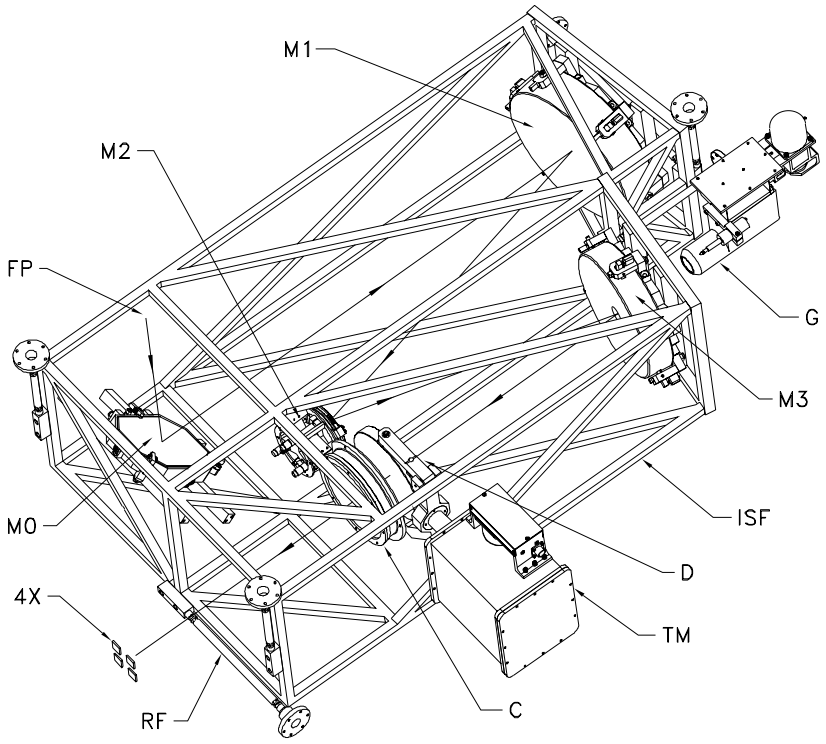

FIG. 4.—CAD drawing showing the Offner optical system within its Invar mount. FP is the telescope focal plane; ISF is the Invar space frame; M0, M1, M2, and M3 are the flat and Offner spherical mirrors; G is the guide camera behind M3; D is the dichroic; C is the corrector; TM is the dichroic angle control gearbox (actually located outside the wall of the dewar; and RF are the rod flexures). The detectors are shown expanded by a factor of 4.

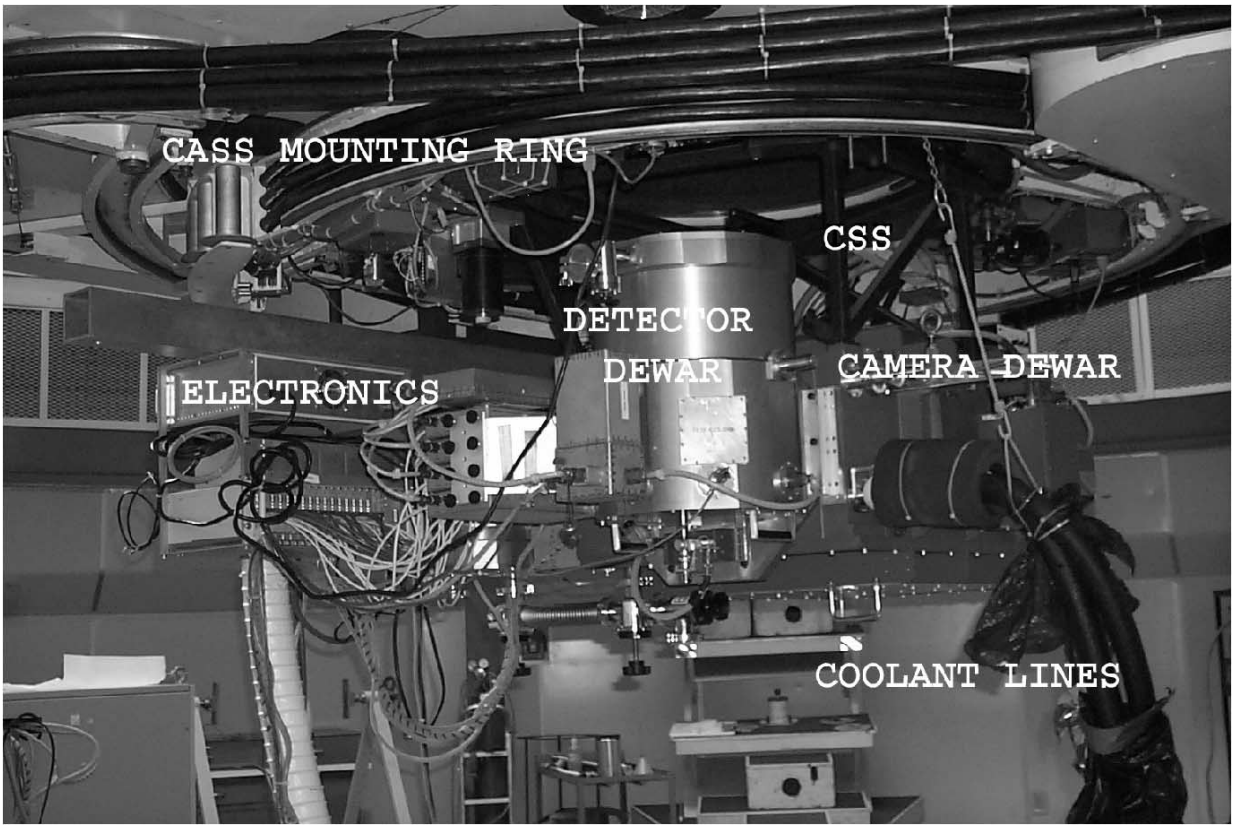

FIG. 5.—Photograph of the outer aluminum dewar, the CSS (space frame), the new detector dewar completed in 2002 February, the detector electronics, and cooling hoses, mounted on the du Pont Telescope. [*See the electronic edition of the Journal for a color version of this figure.*]

Owing to the limited load capacity of the telescope, we tried to minimize the overall weight of the mechanical structures. The total calculated weight of the instrument, not including electronics, is 335 kg.

Detailed mechanical design results are summarized in Tables 3, 4, and 5. Table 3 presents a comparison of the design goals and FEA results for the optical misalignments due to gravity effects upon the ISF. For each spatial axis, the first row shows the specifications developed from the PSF degradation analysis and the second row shows the FEA results for a 1 *g* force along that axis. In all cases, the FEA deflections are well within the specifications. For example, the M1-M2 and M2-M3 focus directions are primarily along the *Y*-axis, and Table 3 shows this to be the most critical alignment direction. The bracketed numbers specify that M1, M2, and M3 should not move by more than 40 μm (i.e., ± 20) with respect to each other. From the calculated motions, M1 moves 7.2 μm (i.e., 29.3–22.1) in the *Y*-direction with respect to M2 for a gravity force change of 1 *g*. Similarly, it is the case for all motion directions that optical elements tend to move together, producing differential motions of roughly a few microns. We concluded that the real ISF would provide more than adequate stiffness under gravity loading.

FEA models were also made to certify the diameter-to-thickness ratios chosen for the mirrors and their mounting fixture designs. Each element was analyzed individually, as subjected to a 1 *g* force perpendicular to its surface. The bot-

TABLE 3

OPTICS ALIGNMENT SPECIFICATIONS AND FEA RESULTS FOR 1 *g* FORCE

Optic Direction	M0 (μm)	M1 (μm)	M2 (μm)	M3 (μm)	Corrector (μm)
X specification[a]	[±50]	[±120]	[+25, −40]	[±90]	[±250]
X FEA	17.7	16.0	12.1	15.7	18.9
Y specification	[±50]	[±20]	[±20]	[±20]	[±250]
Y FEA	25.9	29.3	22.1	24.8	30.0
Z specification	[±50]	[±120]	[±40]	[±120]	[±250]
Z FEA	9.9	15.5	9.1	16.3	13.8
P-V distortion FEA	0.071	0.029	0.008	0.035	0.170 (C1) 0.052 (C2)

[a] The *XYZ* optics alignment specifications were derived from a detailed consideration of the degradation of the PSF as the optical design was perturbed; see § 2.4.

TABLE 4
RIGID-BODY TRANSLATIONS OF OPTICS (FEA)

Force	ΔX (μm)	ΔY (μm)	ΔZ (μm)	$\Delta\Theta(X)$ (arcsec)
Apply vacuum.....	89	178	61	14
Gravity vectors:[a]				
Dewar	142	102	8	...
Rods	8	4	3	...
ISF.....	5	13	3	...
CSS.....	51	24	13	...
Total.....	203	152	25	...

[a] Component displacements of the optical system with respect to the telescope axis, for a 90° rotation through the gravity field.

tom row of Table 3 gives the peak-to-valley (P-V) surface distortions in microns. At the shortest wavelength of operation, viz., 1.0 μm, the largest mirror distortion is $\lambda/14$ (P-V) for a 1 g force; clearly, the optics themselves are diffraction limited with respect to mechanical distortions in actual operation, where most of the force is perpendicular to the axes (for M1, M2, and M3), and the axial force on each mirror is usually less than 0.7 g. In conclusion, our FEA models of the mechanical systems imply that the burden of achieving good optical performance lies with the two issues of fabrication of the optical elements and their static alignment in the lab.

Translations of the camera optical system with respect to the telescope's optical axis arise from distortions of the CSS and dewar and from rigid-body motion of the ISF within the dewar as the telescope points away from the zenith. Table 4 summarizes the FEA results and shows that the dewar and CSS translations are equivalent to only a few arcseconds' pointing error in going from zenith to horizon. Motion of the optical system with respect to the dewar and detector result from deflections of the rod flexures and ISF. These motions cause out-of-focus images of warm dust particles on the dewar window to move around as the telescope tracks. Table 4 shows that these motions should not exceed a few microns, or a fraction of a pixel. Changes in ambient temperature do not misalign the optics either; the resulting dimensional changes produce only rigid-body motions of the ISF, that is, pointing errors. The residual pointing errors are both small and slowly varying and are thus guided out. Flexure between the dichroic, Xybion camera, and detector dewar are small because each of these assemblies is attached to the aluminum outer dewar, *not* to the ISF.

We also used FEA to control deflections at the centers of the dewar walls under vacuum. The design keeps the maximum stress in the dewar walls to a factor of 5 below the material yield strength. The predicted maximum deflection is 0.7 mm, which was confirmed by measurement. Table 4 shows that the resulting distortion produces a rigid-body motion of the ISF assembly of only ~0.14 mm.

2.5. *Mechanisms*

Three mechanisms are used to acquire guide stars and for fast tip-tilt guiding. The dichroic filter is mounted within a gimbal, so that the beam from different subregions within the telescope focal plane can be directed to the guide camera. The gimbal angles are controlled via an evacuated gearbox that contains sets of antibacklash gears and encoder systems, one for each axis. Vacuum feedthroughs (FerroTec Corp.) carry torques from the stepper-motor shaft into the gearbox, and the dichroic is thereby steered under computer control.

Optical light reflected off the dichroic passes through the 19 mm diameter hole in the center of M3, the heat mirror, and the window to the external guide camera. The camera is an intensified CCD system (Xybion Corp.) having a GaAs photosurface 15 × 9 mm in size and operated at a 30 Hz frame rate. It is mounted in a focusing mechanism that provides both manual (coarse) and computer-controlled (fine) adjustment.

The video output of the guide camera is processed in a computer to find the centroid of a stellar image, derive correction signals, and return these to three actuators that tip and tilt mirror M2 (Fig. 6), which is kinematically mounted within the ISF and thermally anchored to it. Axial definition and tip-tilt motions are provided by a push-pull arrangement: three piezoelectric actuators (Physik Instrumente GmbH) contact the back of M2, which is spring-loaded against them. An actuator motion of 2 μm corresponds to an image motion of 1″ at the focal plane, so motions are typically ~0.1 μm.

The actuators are thermally isolated from M2 and the ISF, in order to maintain them at or above −15°C, as recommended by the manufacturer. This was accomplished by clamping the three actuators within an aluminum block, which is stiffly suspended within the M2 alignment mechanism on three thermally resistive G-10 (epoxy-glass) plates. A servo-loop temperature controller (Lake Shore Cryotronics, Inc.) maintains the correct temperature of the aluminum block via a heater resistor clamped into the block and a temperature sensor.

2.6. *Cooling System*

The temperature of the ISF and optics, −40°C, is well within the range of commercial refrigerators and obviates the need for cooling this substantial mass (115 kg) to 77 K with liquid nitrogen (LN_2). We chose a model ULT-95 recirculator (Neslab Instruments Inc.). The heat transfer liquid is Syltherm XLT (Dow Chemical Co.), chosen on the basis of operating temperature range, viscosity, and heat capacity. The refrigerator has a 1600 W maximum cooling capacity, which, however, cannot be realized in practice. Losses are incurred pumping the fluid against gravity, and from thermal loading in the coolant pipes running between the recirculator and the dewar.

The heat transfer liquid is coupled to the ISF by pumping it through a loop of copper pipe that makes a circuit around the ISF after entering the dewar through a vacuum feedthrough. The pipe is fastened to the ISF with spring-loaded clamps at 20 locations. The copper pipe is bent through a series of gentle curves so as to minimize stresses upon the ISF as the copper shrinks thermally. Additional copper clamps and strips attach the entrance and exit baffles, the dichroic, M1, M2, and M3 directly to the copper pipe. The temperatures of the ISF and optics are monitored with five silicon-diode temperature sensors (Lake Shore Cryotronics). The entering and exiting fluid temperatures plus known flow rate allow us to control the rate at which thermal energy is being removed during cool-down, and to generally monitor the thermal environment during observing. The heat content of the cold (−40°C) mass is 4.2 MJ

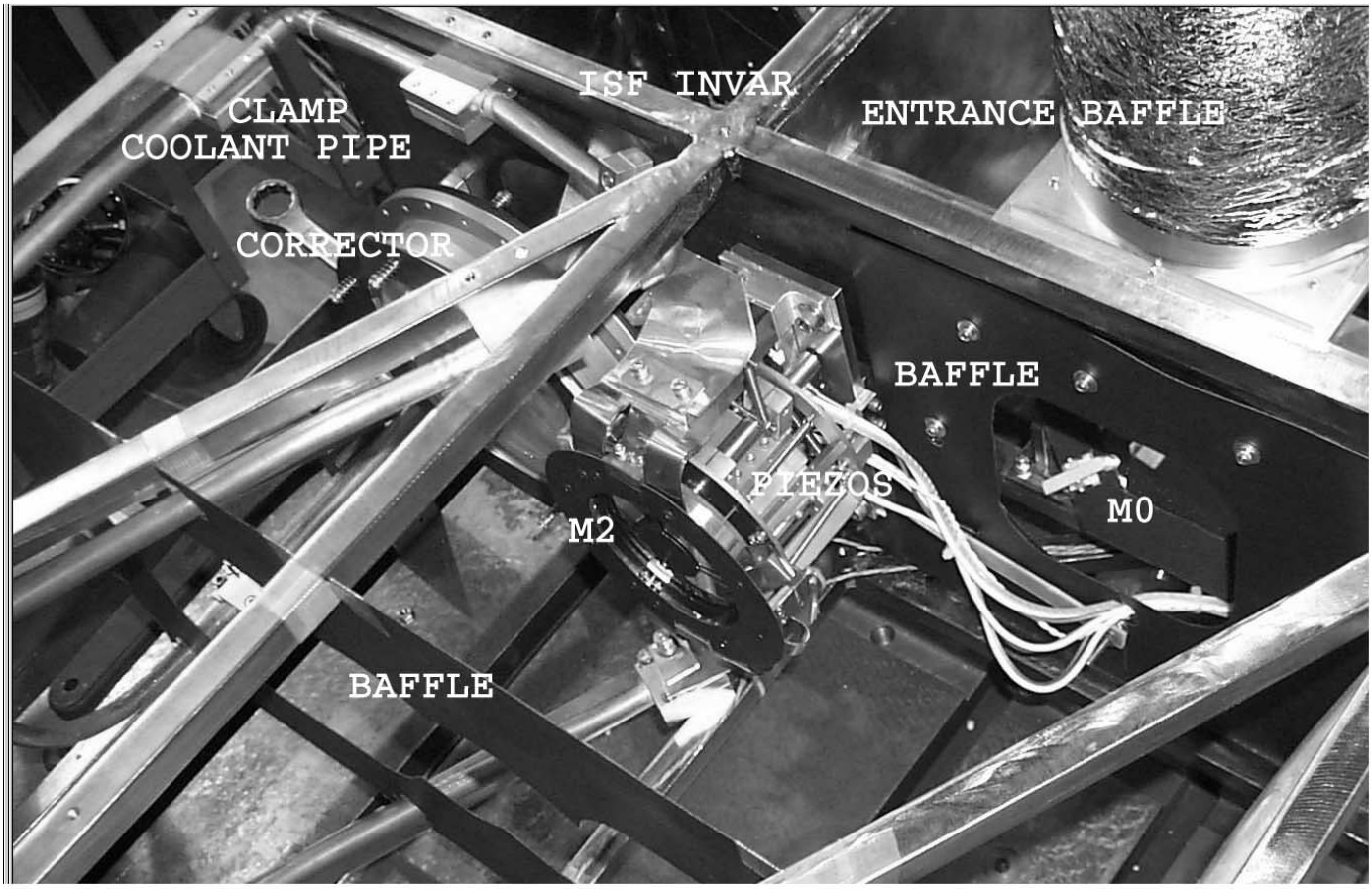

FIG. 6.—Photograph of M2, its baffle masks, and the kinematic mounting within the ISF. Several of the copper cooling pipes, clamps, and straps are shown. The cylinder covered in aluminized Mylar in the upper right corner is the entrance baffle. [*See the electronic edition of the Journal for a color version of this figure.*]

(Table 5), which would imply a cool-down time of less than an hour for perfect thermal coupling and transfer through the materials. In practice, the cool-down time is set by M1, which reaches -35°C in about 24 hr.

2.7. *Radiation Shielding and Optical Baffling*

The total surface area of the inside of the dewar is 2.7 m^2. At 300 K and for an emissivity of 0.05, typical for polished aluminum foil, this surface would supply a net load of 34 W onto a unit-emissivity interior camera-cooling system at 233 K. The latter was shielded by attaching a multilayer stack of aluminized Mylar and an outermost aluminum sheet thermally anchored to the copper pipes taking the heat transfer liquid out of the dewar. The net radiative load upon the camera components within the ISF is thereby reduced to $\sim$5 W.

TABLE 5
SUBSYSTEM MASSES AND HEAT CONTENTS

Subsystem	Mass (kg)	Heat Content (KJ; δT = 60 K)
Mirrors (M0, M1, M2, M3).....	16	777
Mirror support system	74	2300
Refractive optics	3	99
Coolant system	13	436
Baffles	3	148
Radiation shields	7	404
Aluminum dewar	110	...
Mechanisms.....	10	...
Guider	1	...
CIRSI detector dewar	62	...
IR4 detector dewar.....	38	...

Optical baffling, used to reduce stray light within the system, is provided at several points along the optical path: ahead of and behind the entrance window, around the edges of mirrors M0, M1, and M3 and the corrector, and through the interface between the camera dewar and the detector dewar. The innermost walls of the main radiation shield are carbon-fiber epoxy, whose black surface absorbs stray radiation. The most important baffle is at M2. Figure 6 shows how M2 and its masks are thermally anchored to the coolant lines. The masks are of machined aluminum and painted with a flat black aerospace paint. Three effects dilute the intensity of thermal radiation reflected off the mask toward the detector: it has low albedo for pure reflection at 2.3 μm; because its surface is flat, the residual reflected image of the pupil is spread over an area far larger than the detector by M3; and finally, light scattered off its rough surface is absorbed elsewhere within the camera. Because this image has aberrations (see § 2.2), the masks overstop the pupil, allowing 95% of the light through.

2.8. *Optical Alignment in Practice*

The formal alignment tolerances of an Offner are stringent. The most severe aberration in practice is astigmatism, to which the Offner design is quite sensitive. One advantage, however, is that small translations and tilts orthogonal to the focus direction are redundant. The accuracy of the *X*-*Y* alignment (Table 3) is thereby determined mostly by tilting the mirrors accurately, which in practice is simpler than measuring and controlling translations.

Optical alignment was accomplished using a horizontal boring mill, a dial indicator, and a theodolite mounted on a translation stage. First, the approximate mirror vertices were marked and the ISF was mounted on the mill and squared to its axes. The dial indicator was used to locate (to ± 0.5 mm) the vertices of mirrors M1, M2, and M3 and the corrector, along the *Z*-axis. The theodolite, its axis squared to that of the mill, was then used with targets set up at the two focal planes and at the centers of M1 and M3 to set their spacing in *X* and *Y*. The tilts of M1 and M3 were set by viewing a target at the center of M2, and the tilt of M2 was set by making the entrance and exit focal-plane images coincident. The last step was to locate M0 so that an image of the telescope exit pupil was correctly aligned with the mask on M2. The whole procedure was iterated once so that all the vertices were located to ± 100 μm accuracy.

To gauge the image-quality standard, a US Air Force optical target at the first focal plane (see Figs. 2 and 4) was imaged at the exit focal plane and inspected with various high-power eyepieces. We were able to separate the black and white bars of the target at a pattern scale of 130 line pairs per millimeter, corresponding to a bar width of 4 μm, 0.22 of a detector pixel, and $0\farcs05$ at the telescope.

Defocusing of the optics due to the 60°C difference between room alignment and operating temperatures is largely circumvented through the use of Invar for the space frame. Nevertheless, the residual 40 μm of shrinkage in the focus direction was compensated for by including within M2's mount a section of aluminum that shrinks an equal amount in the opposite direction.

The optical axis of the ISF would ideally be accurately aligned to the optical axis of the telescope. This particular alignment is critical, as it determines the placement of the exit-pupil image on the baffle at M2. The adjustment was made with the camera mounted on the telescope but with the dewar lid (which opens down) removed and the ISF and optics fully accessible. By visually inspecting the image of the actual telescope primary formed at M2, we used a combination of tilts and translations of M0 to precisely center the pupil image on M2's centered baffle. The final step was to recenter the two focal planes by translating the telescope focal-plane baffle into alignment with the location of the four arrays.

The alignment mechanism design and procedure were the most painstaking aspects of the camera's development. The laboratory results and on-telescope adjustments indicated that the camera should have a negligible effect upon the images delivered through the atmosphere and telescope, and that the camera should meet its thermal-baffling goals.

3. CAMERA ELECTRONICS

The electronics are logically divided into two separate systems interconnected by control computers: the readout electronics for the imaging arrays, and a set of subsystems that support the guiding, motion control, and camera temperature control functions. The control computers are discussed in § 4.

3.1. *Readout Electronics Design*

The first detector system to be mounted on the camera was CIRSI, the Cambridge Infrared Survey Instrument (Beckett et al. 1998). The LN_2 dewar contains four Rockwell engineering-grade detectors and a filter wheel. We have recently upgraded to four science-grade detectors housed in a newly constructed dewar. The Carnegie-built electronics are common to the two dewars.

The goal was to provide readout electronics with the following attributes: (1) direct digitization of the data and minimum analog design complexity, and accuracy to 16 bits of resolution in terms of read noise, dynamic characteristics, and stability—this ensures that the high quality and low noise potential of the HAWAII arrays are not compromised; (2) ability to support a 4 μs pixel dwell time, the minimum acceptable for science-grade HAWAII devices (based on advice from Rockwell and the results of other groups); (3) a double-correlated readout strategy similar to that commonly used to clock NICMOS3 detectors, to capitalize on our experience and proven circuit designs; (4) enough speed that the overall data system throughput would be determined by the readout rate and not by computer or data transmission bottlenecks; (5) some programmability and flexibility, but within a system that is not totally reconfigurable; (6) ruggedness and reliability, for long-term use and easy service at Las Campanas Observatory.

The system designed and built to meet these goals is diagrammed in Figure 7. A key feature is that all 16 quadrants of the ensemble of four arrays are read out in parallel. This design choice allowed us to avoid the difficult analog design issue of multiplexing a video rate signal with 16 bit accuracy. The output of each HAWAII quadrant is connected to the input of an external low-noise DC amplifier. This single-ended amplifier supplies a source resistor to complete the on-array source-follower FET amplifier, removes the DC bias voltage, and amplifies the resultant pixel voltage by a factor of 10. The amplified signal is fed to its own 16 bit analog-to-digital converter (ADC). After a pixel has been clocked and settled, all 16 ADC conversions are triggered simultaneously. The digital outputs of the ADCs are bussed together onto a custom backplane and strobed into a commercially made 16 bit parallel interface card (PIC; Spectral Instruments, Inc.) operating in one PCI (Peripheral Component Interconnect) slot of the data acquisition computer. This rack-mounted industrial-style computer is a 200 MHz Pentium-based system running Windows 98.

The DC amplifiers use a two-stage (buffer and gain) design based on the OP627 operational amplifier (Burr-Brown Corp.). They are designed to settle to within a 16 bit error band on a full-scale output (-2.5 to $+2.5$ V) within 2.2 μs when driven by a step function at the input. This is more than adequate to meet the goal of a 4 μs settling time and allows for the interesting possibility of oversampling a pixel and digitally filtering the result. (We intend to use this latter capability in future spectrographic applications where read-noise suppression is of paramount importance.) The performance of the amplifiers was calculated by hand and veri-

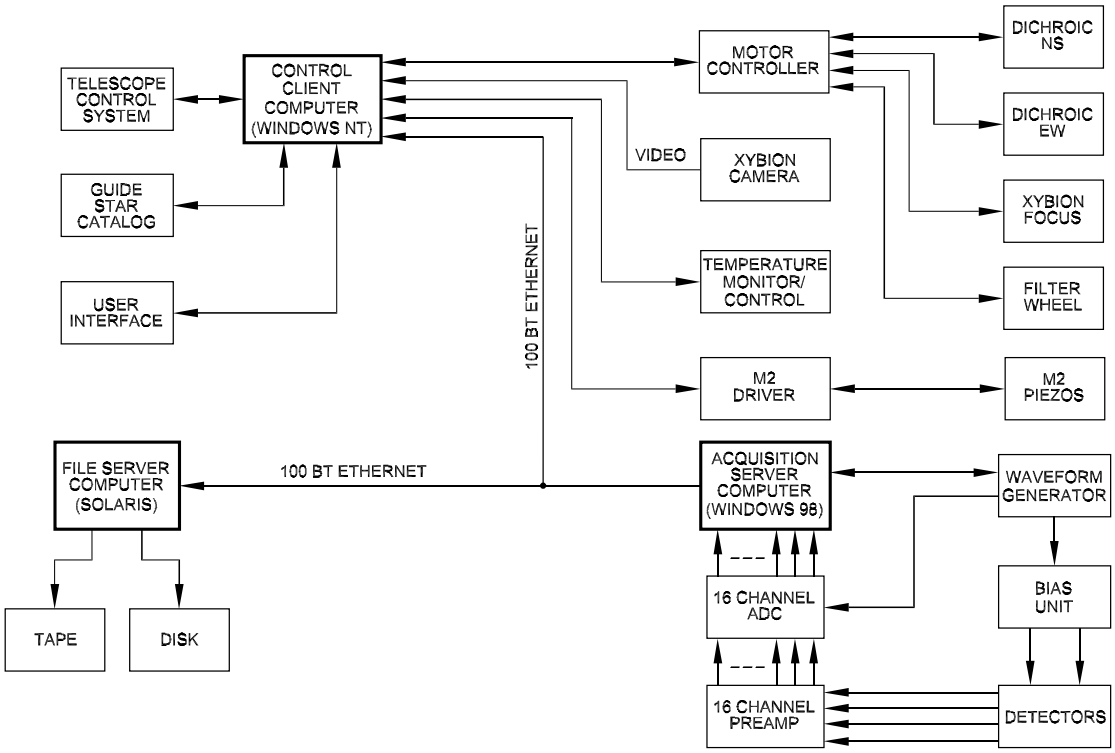

FIG. 7.—Block diagram of the electronic and computer control system. Power suplies have been omitted for clarity. See text for explanation.

fied with the PSpice analog design simulation software (MicroSim Corp.). The amplifiers were built onto individual surface-mount printed circuit (PC) boards; we rigorously followed low-noise layout practices and used the highest-quality construction materials and components reasonably obtainable. The PC boards were mounted into cavities in custom-made enclosures milled out of solid blocks of aluminum, with each cavity holding one amplifier. The purpose of the separated mounts was to isolate the PC boards both from each other and from potential external noise sources. Each milled enclosure contains four amplifiers, enough to service one HAWAII array.

The ADC cards are based on the Analogic 4322, 2 MHZ units (Analogic Corp.). These converters were built onto custom-designed surface-mount PC boards, which operate in an enclosure with a wire-wrapped backplane that implements a custom readout bus. Two additional boards share the backplane: a multiplexer responsible for backplane logic, and a diagnostic interface for debugging purposes. As with the DC amplifiers, close attention to low-noise electronics methodology was followed in designing the ADCs. This included extensive shielding and filtering, opto-isolation of all digital signals into or out of the ADC boards, and the use of linear power supplies. The resulting rms conversion noise is in all cases $\sim$0.7 ADU and close to the ideal value of $\pm$0.5 ADU.

The clocking of the arrays and other synchronous activities are handled by our waveform generator unit (WFG). The design is based on synchronous logic that generates addresses for EPROMs, which in turn store waveforms responsible for generating array clocks, ADC clocks, and strobes for the PIC. The basic idea is that synchronously decoded counters generate addresses for the EPROMs until all clocks are generated for a given array clocking set. The counters then reset automatically, ready for another clocking sequence when so commanded. This circuit is supervised by an 8752 (8051 family) microprocessor, which runs time-critical functions with all interrupts disabled for absolute repeatability. The WFG is essentially a repackaged and reprogrammed version of the circuit described in Murphy et al. (1995).

System voltages are generated in the bias unit, which is responsible for providing stable low-noise analog voltages to power the arrays and related low-level gain-stage circuitry in the amplifiers. The bias unit also opto-isolates the array clocks from the WFG before they are fed into the dewar to the arrays. A description of the bias unit is given in Murphy et al. (1995).

The physical deployment of our electronic units on the telescope is a significant issue and takes into consideration the sensitive nature of some of the signals and interconnections between units and weight, bulk, and heat generation factors. The DC amplifiers and bias unit are mounted directly on the LN_2 dewar holding the arrays. Thus, cable lengths between the lowest-level gain and biasing stages are minimized, and shielding effectiveness is maximized. The ADC subsystem is mounted on the telescope close to the amplifier units. The amplified signals are carried from the preamps over a 40 cm length of low-loss RG-62 coaxial cable to the ADC inputs. The capacitance of this cable (proportional to length) can affect settling time, and keeping it short is important. The WFG is also mounted on the telescope, but $\sim$1 m from the sensitive analog systems. The data acquisition computer and ADC power supplies are located in an instrumentation rack on the telescope dome floor, $\sim$5 m from the dewar. Excess heat is carried away from the ADC chassis via a household clothes-dryer vent hose and out of the telescope dome.

3.2. *Auxiliary Electronics*

A number of additional electronic instruments are deployed to support the instrument; they are shown the block diagram of Figure 7. These are the data acquisition computer, the electronics for controlling the piezo-actuators, the Xybion guide camera and its control electronics, a multichannel cryogenic temperature sensor module, a cryogenic temperature controller for the piezo-actuator mount, linear power supplies for the ADC unit and preamps, fiber optic transceivers for RS-232 communications between the instrument and control room, fiber optic transceivers for fast Ethernet communication between this rack and the control room, and a four-channel motor controller system. The latter interfaces our control computer to the motors for the dichroic gimbals, guide-camera focus, and filter wheel.

4. COMPUTER DATA SYSTEM

4.1. *Requirements*

Because the instrument was intended primarily for extensive survey work of a repetitive nature, essentially automatic data acquisition was designed in from the start. This includes scripted guide-star acquisition and guiding, telescope moves, filter changes, and detector reads.

Faced with the significant hardware and software challenges of developing a distributed data system capable of meeting our goals, we decided to take advantage of industrial standards as much as possible and to adopt off-the-shelf solutions for interfacing instruments. Primary among these goals was to avoid the development of either custom-built interface cards or custom-written device drivers, both costly and labor-intensive endeavors.

The computer system provides the following main functions: (1) Tools to acquire and store the data from the readout electronics. Contained within this software is a macro language that allows the observer to construct a script of arbitrary length containing combinations of filter changes, exposures, telescope moves, and compensating guider moves. (2) An interface to control telescope pointing, offsets, focus, filter wheel position, and the fast guiding camera subsystem. (3) An astrometric tool set and star catalog database to assist the observer in quickly finding guide stars and in developing and implementing efficient observing procedures. (4) An interface for monitoring the thermal state of the dewar, detector arrays, and the M2/piezo tip-tilt subsystem. (5) An on-line data reduction system based on IRAF scripts, plus other familiar Unix-based analysis tools and system utilities.

4.2. *Implementation*

The architecture is shown in Figure 7. Three computers communicate with each other through 100Base-T Ethernet on their own switched segments. The computers are designated the Control Client, located in the telescope control room; the File Server, also located in the control room; and the Acquisition Server, located in a 19 inch (48 cm) rack-mounted enclosure on the telescope dome floor. Each computer runs a different operating system. The Control Client is a 200 MHz Pentium-based PCI passive-backplane industrial-style rack-mounted computer with a 2 Gbyte SCSI drive, 128 Mbyte of RAM, and a digital audio tape (DAT) unit, and it runs Windows NT Workstation 4.0. The Acquisition Server is a 750 MHz Pentium-based passive PCI backplane industrial-style rack-mounted computer with a SCSI disk, 128 Mbyte of RAM, and a DAT drive, running Windows 98. The File Server is a Sun Ultra 2 with three SCSI disks, a DAT drive, and 384 Mbyte of memory. The File Server runs Solaris Unix.

The overall function of the system may be described most clearly in client-server nomenclature. The Acquisition Server is a server for client requests to generate data frames from the camera. These requests are initiated over TCP/IP sockets and originate from GUI-based client software running on the Control Client. These client requests result in double-correlated images complete with FITS headers, which are written to the File Server. The File Server uses the Server Message Block (SMB) protocol and Samba server software to make its shared volumes available to the Acquisition Server. Observers log on locally to the File Server to analyze the incoming images with IRAF, run reduction scripts, display samples of the data, and perform data management and storage functions.

The Control Client computer is not only in charge of initiating data acquisition, but commands the entire guiding process and takes control of the telescope by providing it with offsets for mapping image mosaics on the sky. The Control Client usually runs a scripted observing sequence to perform long mosaicking operations consisting of several positions on the sky, with numerous dithers at each position. The system is capable of acquiring data and running autonomously, including guide-star acquisition, for sequences up to 6 hr long. The system is able to take exposures without bottlenecks at a continuous rate of about one double-correlated picture (for all four arrays) per 10 s, that is, a data rate of $\approx$1 Mbyte s^{-1}.

An important software tool that maintains high observing efficiency is the guide-star search-and-display program. It takes only 2 seconds for this application to search through a database of 50 million stars (preselected from several combined star catalogs) and to return a set of $\sim$10 stars within the available guide field. The dichroic is quickly rotated to aim the guide camera at the best star, and the automatic data acquisition sequence is launched.

An important feature inherent in our adopted architecture is ease of diagnosing problems. To test the electronics and to perform array characterization, we use a Diagnostic Client, essentially a small GUI-based Windows application that connects to the Acquisition Server's socket interface, but which offers greater control of the details of the readout process (i.e., clocking options) and a quick look at samples of raw data. The Diagnostic Client serves to exercise and test the entire hardware-software system from an engineering point of view.

Despite the complexity of the system, and the variety of instruments and interfaces under computer control, we were able to entirely avoid writing device drivers. We developed all the necessary code using a single industry-standard language and compiler, Microsoft Visual C. The development effort consumed approximately 4 man-years of coding.

5. CAMERA PERFORMANCE

Our quoted performance results pertain to the CIRSI detectors, which are early generation engineering-grade devices and not up to Rockwell's current (year 2001) stand-

ards for science-grade devices in terms of quantum efficiency (QE), QE dispersion, and bad-pixel count. Other gains that have resulted from the installation of the science-grade detectors involve robustness in the data processing and, consequently, the final data product. These include the detection and elimination of dead or "hot" pixels and improved sky subtraction resulting from smaller sensitivity variations across the arrays.

5.1. *Electronics Performance*

The detector electronics perform well in that they add negligible excess random or pattern noise to the inherent read noise of the arrays themselves. Our measured read noise is 15 e^- rms for a double-correlated picture. The DC amplifier, ADC, power, and grounding designs were therefore deemed successful.

We followed Rockwell's guidelines of keeping the pixel clocking rate at ~100 kHz. We read each 512 × 512 quadrant in 2 s, which is 130 kHz. The penalty for reading faster than this is to introduce unstable rolling bias levels that do not completely disappear when sky pictures are subtracted from data frames. Also, we have found empirically that by performing a single nondestructive clocking of the full array *before* the double-correlated clockings, any residual bias gradients in the differenced frames are reduced to negligible levels.

5.2. *Image Quality*

Much attention was paid in the optical and mechanical design work to maintaining good image quality. Our assessment in the laboratory was that the camera image quality was excellent and is a better indication of the intrinsic PSF than images obtained on the telescope. With a few tens of nights of experience with the system as a whole, we are convinced that the camera is not degrading the seeing-dominated PSF at all. With the tip-tilt system in operation, the best image quality we have measured is 0.″38 FWHM at K_s for a 45 s exposure. The image-quality budget has contributions from telescope diffraction (~0.″2) and astigmatism (also ~0.″2), so the 0.″38 number confirms that the camera optics *must* be excellent. Under good seeing conditions (FWHM ~ 0.″45), we often notice that the image profiles of stars are systematically peaked at the central pixel, as though some energy from the body of the profile is being shifted into the diffraction-limited core. This effect is to be expected to some degree. For 0.″5 FWHM visual seeing, Fried's (1966) parameter r_0 will be ~1 m at 2.2 μm. There are thus of order (only) a few r_0-sized coherent wavefront patches over the entrance pupil, and some degree of first-order adaptive optics effect should be realized. Our conclusion is that the tip-tilt system plus the excellent intrinsic image quality of the camera have allowed us to realize the best possible imaging potential of the 2.5 m telescope to date.

5.3. *Throughput*

The system throughput can be defined in several ways, depending on whether one includes the atmosphere, telescope, and array QE. What matters most in designing observations is the detector output (in electrons) per photon onto the unblocked annulus of the telescope primary mirror, projected to the top of the atmosphere. It thus includes the atmosphere, telescope, dewar window, camera mirrors, dichroic, corrector, filter, and detector. The expected throughput has been computed from the data sheets for the various components provided by their manufacturers and estimated for those for which we lack hard data. The computation was carried out using digitized transmission, reflectivity, or QE functions at 10 Å spacing. Table 6 gives the average throughput values for the various individual elements in the optical path and thus contains the different definitions of throughput.

TABLE 6
SYSTEM THROUGHPUT COMPARISONS

Element	J	H	K_s	Note
Wavelength (μm)	1.25	1.65	2.16	
$\Delta\lambda$ (μm)	0.224	0.294	0.324	1
Atmosphere	0.852	0.950	0.878	2
Telescope	0.874	0.893	0.907	3
Camera:				
Window	0.966	0.998	0.972	4
M0	0.987	0.991	0.989	5
M1	0.986	0.990	0.991	5
M2	0.940	0.944	0.945	6
M3	0.971	0.975	0.976	7
Dichroic	0.955	0.930	0.915	8
Corrector	0.975	0.949	0.974	5
Filter	0.892	0.864	0.895	9
Total	0.720	0.688	0.701	
Detector QE	0.63	0.63	0.68	10
Throughput expected	0.41	0.47	0.47	11
Throughput measured	0.45	0.50	0.50	

NOTES.—(1) $\Delta\lambda$ used to compute incident stellar flux. (2) Mauna Kea atmosphere at sec $Z = 2$; assumed equivalent to Las Campanas atmosphere at sec $Z = 1.2$. (3) The telescope mirror reflectivities are estimates based on time since aluminizing and visual appearance of surface dust layer. (4) Data from Crystal Systems, Inc. (5) Data from JML Optical Industries, Inc. (6) Includes undersizing of mask on M2. (7) Includes 1.5% vignetting by central hole. (8) Data from Barr Associates, Inc. (9) Filter transmissions from Barr Associates (J), OCLI (H, K_s). (10) Data from Rockwell Science Center. (11) The straight products of the throughput factors for each component are lower than the expected values because the filter passband edges remove regions of lower atmospheric transmission. Detailed convolutions of the response functions, as have been done for these entries, are required to yield correct expected throughputs.

The *measured* throughput requires knowledge of the electronic gain of the detector-amplifier-ADC combination; this was determined using a standard noise-versus-signal analysis. Under nominal observing conditions of transparency and telescope mirror reflectivities, we measured the throughputs given in Table 6. The expected and measured throughput values for the total light path are in good agreement, but the measured values are a few percent better than expected. We attribute this, without proof, to the fact that the transmission of multilayer coatings often tends to improve slightly at low temperatures. If such effects are at work in the filter, dichroic, and lens coatings, then the measured and expected throughputs probably do agree very well.

5.4. *Sky and Telescope Backgrounds: Measurement Limits*

The depths of JHK_s observations carried out with this instrument depend on the sky and telescope background levels and negligibly on read noise. As is well known, OH emission from the upper atmosphere is strong and highly variable, especially at H (see, e.g., Oliva & Origlia 1992).

TABLE 7
Sky-plus-Telescope Backgrounds and Limiting Magnitudes (Air Mass = 1.2)

Conditions	J	H	K_s	Notes
Background (low OH, 0°C) (mag arcsec^{-2})	16.0	14.7	13.8	1, 2
Background (high OH, 12°C) (mag arcsec^{-2})	15.7	14.1	13.1	3, 4
Limiting magnitude (low OH, 0°C) (mag)	22.6	21.4	20.8	5
Limiting magnitude (high OH, 12°C) (mag)	22.4	21.1	20.5	

Notes.—(1) The lowest OH sky emission typically occurs in the middle of the night. (2) Zero degrees Celsius is as cold as it gets at Las Campanas in June, July, or August. (3) High OH emission refers to maximum H-band background. (4) Typical ambient temperature is 12°C. Calculation of the expected change of K_s background with ambient temperature is consistent with the measured drop of 0.06 mag per degree Celsius shown in the table. (5) Limiting magnitudes are on the Vega system and refer to a 5 σ measurement of a point source within a 2″-diameter aperture in a 1 hr exposure.

Table 7 gives representative numbers as measured over the last decade at Las Campanas. By making direct comparisons of the backgrounds as measured at the 2.5 m and 1 m telescopes simultaneously, we confirmed that the camera contributes zero excess K_s background.

Detection and measurement limits can shift up or down by several tenths of a magnitude, depending on whether one is measuring spatially extended galaxies or stars in a sufficiently dense field that the PSF can be determined well. For the latter, small measurement apertures plus accurate corrections can be used to extend the data faintward. In the stellar case the limit will grow fainter with better seeing, while in the galaxy case aperture corrections will brighten the limit. For example, Chen et al. (2002) have determined completeness limits for galaxy detections at H in the Las Campanas Infrared Survey. As we accumulate more JHK_s data, the limiting magnitudes will become better determined.

TABLE 8
On-Sky Efficiency Example

Function	Time (s)	Number	Total (s)
Array reset, preread, readout	6	108 (3 × 9 × 4)	648
Exposure time	45	108 (3 × 9 × 4)	4860
Arithmetic	1	108 (3 × 9 × 4)	108
No. of identical exposures	0	3	0
Telescope small moves	5	36 (9 × 4)	180
Telescope big moves	30	4	120
Disk write	10	1	10
Expected efficiency(4860/5926)	82%		
Measured efficiency	78%		

5.5. *On-Sky Efficiency*

We characterize the observing efficiency of our system as the amount of time an observing sequence actually spends exposing on the sky, divided by the total elapsed time, which includes array clocking overheads and telescope dithering and rastering motions. Table 8 lists the various overheads for a sample deep measurement at K_s. Owing to the fixed overhead in reading out the arrays, longer exposure times are advantageous; on the other hand, it is important to collect at least three identical exposures at each telescope position for cosmic-ray removal. For typical observing programs, we are currently measuring an open-shutter efficiency of 76%. In such a sequence, we map a 170 arcmin^2 tile (see Fig. 1) in the K_s passband. This takes an entire summer night with 6.5 hr of open-shutter science time, with the rest of the time being spent on clocking overheads, telescope slewing, focusing, and observing standard stars.

5.6. *A Sample Reduced Frame and a Note on Data Reduction Pipelines*

Figure 8 shows a fully processed tile in the K_s band. The total integration time at each pixel was 12,300 s. The observations were made as part of an extensive survey for faint galaxies (McCarthy et al. 2001; Chen et al. 2002).

TABLE 9
Vendors

Component	Vendor
Analog design software (PSpice)	MicroSim Corp., Irvine, California
Analog-to-digital converters (4322)	Analogic Corp., Wakefield, Massachusetts
Detectors	Rockwell Science Center, Thousand Oaks, California
Dichroic	Barr Associates, Inc., Westford, Massachusetts
Guide camera	Xybion Corp., San Diego, California
Filters (OCLI)	Optical Coating Laboratory, Inc., Santa Rosa, California
Heat transfer liquid	Dow Chemical Co., Midland, Michigan
Mirrors and corrector	JML Optical Industries, Inc., Rochester, New York
Optical ray-tracing package (ZEMAX)	Focus Software, Inc., Tucson, Arizona
Operational amplifiers (OP627)	Burr-Brown Corp., Tucson, Arizona
Parallel interface card	Spectral Instruments, Inc., Tucson, Arizona
Piezoelectric actuators	Physik Instrumente/Poly-Tec PI, Tustin, California
Refrigerator	Neslab Instruments Inc., Portsmouth, New Hampshire
Sapphire window	Crystal Systems, Inc., New York, New York
Temperature control	Lake Shore Crytronics, Inc., Westerville, Ohio
Vacuum feedthroughs	FerroTec Corp., Nashua, New Hampshire

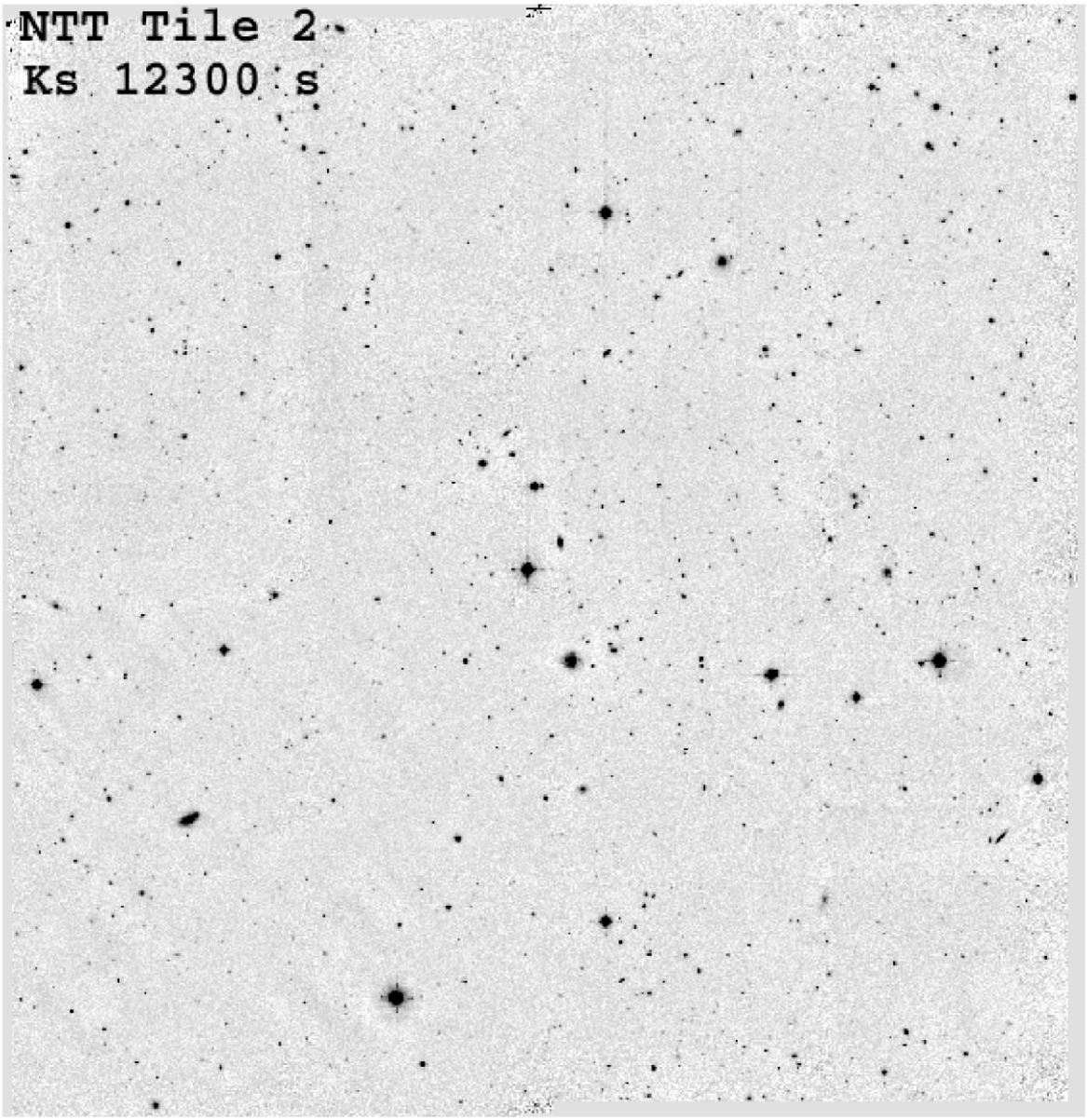

FIG. 8.—Completely processed K_s tile. The exposure time per pixel was 12,300 s. The 5 σ depth in a 2″-diameter aperture is $K_s = 21.1$ mag. This image was taken under rather unfavorable conditions of ambient temperature (15°C) and cleanliness of the telescope primary mirror.

Cosmetically, the final data product is quite satisfactory: fringing and thermal background patterns have been eliminated, quadrant boundaries have virtually disappeared, and there are no signs of electronic artifacts such as rolling bias levels or clumps of dead or hot pixels. The limiting 5 σ magnitude in a 2″-diameter aperture is 21.1 mag; these are roughly the magnitudes of the hundreds of faint galaxies visible in the image. Stellar photometry reaches fainter, as one can obtain an accurate PSF from the brighter stars and use a PSF-fitting program such as DAOPHOT or DoPHOT to extend the depth several tenths of a magnitude. The depth at K_s results in part from the tight PSF, which, averaged over the entire frame, is 0.″7 FWHM.

Figure 8 was produced by a (nearly) automated reduction pipeline, a discussion of which is beyond the scope of this paper. A complete description is given by Chen et al. (2002). Different observational programs will use data reduction pipelines that differ in various ways, depending largely on how the background sky frames are to be computed. One aspect that is common to most observational projects, however, is the virtual necessity of using a robust and efficient pipeline to handle the large quantity of data generated. A related important design consideration is to develop the data acquisition and reduction procedures together as a unit. Optimal processing of infrared array data into a usable scientific product depends upon these two tasks being very tightly coupled, and our faint-galaxy pipeline reflects this philosophy.

It is a pleasure to thank the Rockwell scientists and engineers Kadri Vural, Craig Cabelli, and Scott Cabelli, and the many physicists, managers, and technicians behind the scenes for their efforts. Pat McCarthy and Gus Oemler made vital contributions at various stages of this project.

The following people have made contributions of various kinds to the success of this instrument and the scientific programs thereby enabled: Ray Carlberg and Ron Marzke designed the observational program to measure the galaxy clustering signal; Ken Clardy wrote much of the data acquisition software; Martin Beckett and Craig Mackay made essential contributions toward getting CIRSI operational and keeping it maintained; Miguel Roth and Oscar Duhalde provided essential help at Las Campanas. It is also a pleasure to thank our machinists, Robert Storts, Estuardo Vasquez, and Pilar Ramirez; our technician, Darrell Gilliam; and our support people in Pasadena, Steve Wilson, Scott Rubel, Earl Harris, Greg Ortiz, Jeanette Stone, and Sharon Kelly. The development of the science-grade detector system and associated electronics was supported by the National Science Foundation through its Major Research Instrumentation program. Essential funding from the University of Toronto is gratefully acknowledged. The use of CIRSI, the efforts of Richard Ellis, and the support of the Sackler Foundation is also much appreciated.

APPENDIX

Accurate system transmission functions for the passbands presently in use in the camera are necessary for calculating synthetic colors for different input energy distributions. Of particular interest for the deep extragalactic surveys for which the camera was designed are those combinations of colors that lead to photometric redshift estimates. Figure 9 shows the complete system throughput as function of wavelength for the J, H, and K_s bands. It includes an average atmosphere, all the camera optics, and the HAWAII detector QE. The absolute levels of the throughput are not known precisely, because the HAWAII detector QE values are not known to better than 10%. The plotted curve can be retrieved in digital form, along with all the individual data points that were combined to produce it, from http://www.lco.cl/lco/instruments/manuals/ir/wirc/index.html.

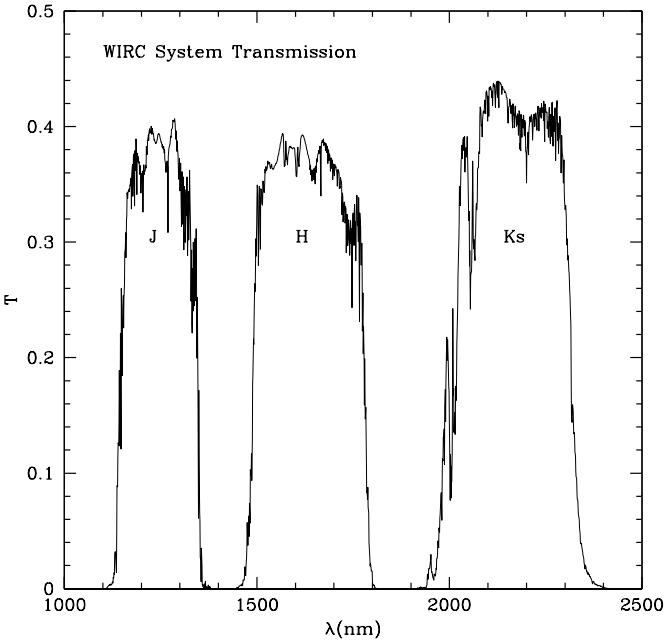

FIG. 9.—System throughput as function of wavelength for the J, H, and K_s bands presently in use in WIRC. They include an average atmosphere, camera optics, and a nominal HAWAII detector QE. The absolute levels of the throughput are not known to better than 10%. See text for how to retrieve the throughput curves in digital form.

REFERENCES

Beckett, M. G., Mackay, C. D., McMahon, R. G., Parry, I. R., Ellis, R. S., Chan, S. J., & Hoenig, M. 1998, Proc. SPIE, 3354, 431
Bowen, I. S., & Vaughan, A. H., Jr. 1973, Appl. Opt., 12, 1430
Chen, H.-W., et al. 2002, ApJ, 570, 54
Fried, D. L. 1966, J. Opt. Soc. Am., 56, 1372
McCarthy, P. J., et al. 2001, ApJ, 560, L131
Murphy, D. C. 1994, in Infrared Astronomy with Arrays: The Next Generation, ed. I. S. McLean (Dordrecht: Kluwer), 301
Murphy, D. C., Persson, S. E., Pahre, M. A., Sivaramakrishnan, A., & Djorgovski, S. G. 1995, PASP, 107, 1234
Offner, A. 1975, Opt. Eng., 14, 130
Oliva, E., & Origlia, L. 1992, A&A, 254, 466